Direct numerical simulation of canonical shock/turbulence interaction

By J. Larsson

1. Motivation and objectives

Shock/turbulence interaction is a fundamental phenomenon in fluid mechanics that occurs in a wide range of interesting problems in various disciplines of science. Examples include supernovae explosions, inertial confinement fusion, hypersonic flight and propulsion, and shockwave lithotripsy (used to break up kidney stones). In many such applications the shock/turbulence interaction includes additional complexities, e.g., real gas effects, multiple species, non-uniform mean flow, or streamline curvature. The most fundamental problem, where these additional complexities have been removed, is arguably that of isotropic turbulence passing through a nominally normal shockwave in a perfect gas. Given the historical success in studying building-block problems in fluid mechanics, canonical shock/turbulence interaction is the focus of the present study.

Ribner (1954) studied the problem analytically by solving the linearized Euler equations with linearized shock jump conditions for incoming purely vortical turbulence. This linear interaction analysis (LIA) relies on several assumptions, most notably that the turbulence comprises a small perturbation relative to the shock and that nonlinear effects in the post-shock evolution are small (as well as the standard assumption of a difference in time scales). Rapid distortion theory (RDT) relies on the same assumptions, but additionally neglects both the post-shock linear evolution and all effects of the turbulence on the shock. In addition, the Rankine-Hugoniot shock jump conditions are incorporated into LIA but not RDT; one consequence is that LIA captures the generation of sound and entropy waves from incoming purely vortical turbulence.

Lee *et al.* (1993, 1997) performed a set of landmark direct numerical simulations (DNS) of canonical shock/turbulence interaction. The first of these papers considered shocks at Mach numbers up to 1.2 where the viscous structure of the shock was resolved; these were therefore truly direct solutions of the Navier-Stokes equations. In the second paper they verified that these "true" DNS results at Mach 1.2 could be replicated by instead capturing the shock (at considerably lower cost), provided sufficient grid resolution in the shock-normal direction at the shock. This methodology was then used to compute cases at Mach numbers up to 3. When comparing the results to LIA predictions, they found that LIA realistically represents many features, including the amplification of transverse vorticity, the amplification and post-shock evolution of the Reynolds stresses, and the decrease in transverse Taylor length scale.

The present study builds on these previous studies by Lee *et al.*. In this paper, DNS in the extended sense of capturing the shock while directly resolving all scales of turbulence is used. It will be shown that a simple argument about the Kolmogorov scale implies that DNS (with a captured shock) requires a refined grid in both the shock-normal *and* the transverse directions to fully resolve the viscous scales of turbulence. This is verified by a grid convergence study, and implies that the calculations in Lee *et al.* (1997) were, most likely, under-resolved. The present DNS data is fully resolved, which leads to larger

differences between the data and LIA. The Reynolds stresses are more anisotropic in the present DNS, and there are qualitative differences in the Taylor length scales. This raises the interesting question of whether under-resolution of the post-shock turbulence in DNS essentially neglects some phenomenon that is also neglected in the LIA. This will be explored below.

The second focus of the present study is the instantaneous picture of shock/turbulence interaction, and how this changes as the degree of nonlinearity (broadly, the strength of the turbulence relative to the strength of the shock) is increased. Zank *et al.* (2002) argued that the nonlinearity of shock/turbulence interaction should be taken into account in analytical theories, and developed a simple model based on the inviscid Burger's equation. Given a jump in mean velocities, the model quantitatively predicts increased mean shock speed and decreased turbulence amplification ratio as the incoming turbulence intensity is increased. In addition, the model predicts that the shock becomes unstable at a critical turbulence intensity.

Hesselink & Sturtevant (1988) performed experiments where a normal shock propagated through a region of randomly mixed helium and R12, and documented instantaneous pressure profiles through the shock that were drastically different from the classical picture. They found what they called "peaked" and "rounded" profiles, and explained these features by shock focusing in the random medium. Interestingly, the same features appear in the present DNS data as well, especially at higher levels of nonlinearity. This raises at least two possibilities: either that nonlinearity in a single fluid problem gives rise to similar dynamics as shock focusing in a two-fluid medium, or that these peaked and rounded profiles really are effects of nonlinearity and not directly a multi-fluid effect. Hesselink and Sturtevant did not document the velocity fluctuations induced by the array of jets used to create the random medium, and the present DNS data is for a single fluid only. Thus we do not attempt to answer the above question here, but rather look for dynamical effects behind the qualitatively different instantaneous profiles.

Throughout this paper the subscripts "u" and "d" refer to average states upstream and downstream of the shock, respectively. For quantities that evolve in the streamwise direction, these states are obtained by extrapolation to the average shock location. The mean flow and turbulent Mach numbers are defined as $M = u_{1,\mathrm{u}}/c_\mathrm{u}$ and $M_t = \sqrt{\overline{\langle u_i' u_i' \rangle}_\mathrm{u}}/c_\mathrm{u}$, respectively, where c is the speed of sound.

2. Numerical method

The compressible Navier-Stokes equations for a perfect gas with ratio of specific heats $\gamma = 1.4$ are solved using a solution-adaptive finite difference method (Larsson *et al.* 2007). Near shocks, a fifth-order accurate weighted essentially non-oscillatory (WENO) scheme is used to approximate the inviscid fluxes, whereas a sixth-order accurate central difference scheme on the split form by Ducros *et al.* (2000) is used in the remainder of the domain. The sensor $s = -\theta/(|\theta| + \sqrt{\omega_j \omega_j})$ is used to identify regions of shockwaves at every time step, where $\theta = \partial_j u_j$ is the dilatation and $\omega_i = \epsilon_{ijk}\partial_j u_k$ is the vorticity. The WENO scheme is applied in regions of $s > 0.5$. Note that the WENO scheme is applied in all directions, which was found necessary for stable calculations at higher values of M_t. This solution-adaptivity leads to a method that captures the shocks in a crisp and accurate fashion while introducing only minimal amounts of numerical dissipation. This was shown by Larsson *et al.* (2007) to lead to a broad range of well-resolved scales. The viscosity is assumed to follow the power-law $\mu = \mu_\mathrm{ref}\,(T/T_\mathrm{ref})^{3/4}$; the Prandtl number

is taken as $Pr = 0.7$. The viscous terms are treated by a sixth-order central scheme, and the system is integrated in time using a fourth-order accurate Runge-Kutta method. The solution-adaptive method introduces internal interfaces between the central and WENO schemes; these are treated in a way similar to that devised by Pirozzoli (2002) to ensure conservation of mass, momentum and total energy. The numerical stability of these internal interfaces was analyzed by Larsson & Gustafsson (2008), where it was shown that the full (coupled) method is linearly stable. Thus any spurious oscillations introduced by the solution-adaptive switching of schemes are bounded. The code has been thoroughly verified on several benchmark problems.

All computational studies necessarily involve various sources of error, and it is essential to analyze and quantify their impact. This is especially true for canonical shock/turbulence interaction, which despite its geometrical simplicity has some very subtle potential sources of error. In the following subsections we consider those elements of the problem that have the largest influence on the accuracy of the results.

2.1. *Inflow turbulence*

It is important to ensure that the turbulence immediately upstream of the shock is realistic, fully developed and well-characterized. In the present study the inflow turbulence is generated in several steps to meet these criteria, essentially following the technique proposed by Xiong *et al.* (2004). First, several independent but statistically identical fields of isotropic turbulence in periodic boxes are generated using the methodology proposed by Ristorcelli & Blaisdell (1997). These fields have exponentially decaying velocity spectra $E(k) \sim k^4 \exp\left(-2k^2/k_0^2\right)$, with peak energy at wavenumber $k_0 = 4$ and microscale Reynolds number $Re_\lambda = \rho\lambda u'/\mu = 140$, where λ is the Taylor length scale which is defined below in Eq. (3.1). They are then allowed to decay temporally (i.e., in periodic boxes) for approximately three eddy turnover times λ/u', which ensures that the turbulence is fully developed and realistic. These independent realizations (or snapshots) of turbulence are then blended together into a longer inflow database, which is then used together with Taylor's hypothesis to specify the time-dependent inflow turbulence. This technique leads to very accurate spatially decaying turbulence immediately behind the inlet (Xiong *et al.* 2004; Larsson 2008). After the decay, the Reynolds number immediately upstream of the shock is $Re_\lambda \approx 40$.

2.2. *Outflow boundary condition*

The flow behind the shock is subsonic, and thus one must take care not to generate acoustic reflections from the outflow boundary condition. This is accomplished through a sponge region that damps the solution toward a quiescent state before reaching the boundary. Terms of the form

$$-\sigma \left(\frac{x_1 - x_{1,\mathrm{sp}}}{x_{1,\max} - x_{1,\mathrm{sp}}} \right)^2 (f - \langle f \rangle_{yz})$$

are added to the Navier-Stokes equations, where σ is a constant, $x_{1,\mathrm{sp}}$ is the beginning of the sponge region, $x_{1,\max}$ is the end of the domain, $f = \rho, \rho u_i, \rho e_0$ denotes each conserved variable and $\langle \cdot \rangle_{yz}$ denotes an average in the transverse directions. We note that this form of the sponge terms does not require knowledge of the average state at the outlet.

The issue of avoiding acoustic reflections from an outflow is common in the literature; however, the more interesting issue is instead that of specifying the back pressure p_∞ such that the shock is stationary in the mean. The Rankine-Hugoniot relations are only valid instantaneously, but not on average in a turbulent flow; they can therefore not be

used to find the p_∞ that yields a stationary shock. Lele (1992) used RDT to develop approximate shock relations for turbulent flow, and found that the density and pressure jumps decrease in the presence of turbulence for a given shock Mach number. Thus the p_∞ that yields a stationary shock (for given M and M_t) should be slightly lower than that predicted by the laminar Rankine-Hugoniot relations. There is, however, one additional effect that counteracts this: the decay of turbulence kinetic energy implies a spatially increasing internal energy, which causes the outlet state to be different from the state immediately downstream of the shock. More specifically, it suggests that the p_∞ which yields a stationary shock is slightly higher than that given by the turbulent shock jump.

In light of these issues, it is clearly difficult to specify the correct p_∞ *a priori*. In the present study we therefore proceed by first computing each case on a coarse grid with p_∞ given by the laminar Rankine-Hugoniot conditions, and computing the resulting average shockspeed U_s. Expanding the pressure jump condition around a small shockspeed yields $\Delta p_\infty \approx 4\rho_\mathrm{u}\, u_{1,\mathrm{u}}\, U_s/(\gamma{+}1)$, which is then used to adjust the back pressure for the fine grid runs. In practice this adjustment is only needed for higher values of the turbulent Mach number. Note that this adjustment makes intuitive sense, in that a positive shockspeed (shock moving toward the outlet) leads to an increase in the back pressure.

2.3. *Grid sensitivity*

Direct numerical simulation of turbulence requires that the viscous dissipation is fully resolved. Denoting the maximum resolved wavenumber as k_max, this typically requires $k_\mathrm{max}\eta \gtrsim 1.5$ (cf. Pope 2000), where $\eta = \left(\nu^3/\varepsilon\right)^{1/4}$ is the Kolmogorov length scale and ν and ε are the kinematic viscosity and rate of dissipation of kinetic energy, respectively. This estimate is applicable to isotropic turbulence, or possibly turbulence that is only locally isotropic (i.e., isotropic at the smallest scales). The turbulence in canonical shock/turbulence interaction is isotropic upstream of the shock, and axisymmetric and out of equilibrium immediately downstream of the shock. It is not clear *a priori* whether the turbulence returns to isotropy. The present DNS data shows that the vorticity components become isotropic at $k_0 x_1 \approx 10$, whereas the Reynolds stresses stay anisotropic (axisymmetric) throughout the domain (discussed below; shown in Fig. 5). Given that vorticity is primarily associated with small-scale motions, one could argue that the concept of the Kolmogorov scale and its relation to the grid resolution makes sense upstream of the shock ($x_1 < 0$) and for $k_0 x_1 \gtrsim 10$. A first assessment of the necessary grid resolution is done by considering the requirement $k_\mathrm{max}\eta \gtrsim 1.5$ in these regions.

Consider the approximate scaling of the Kolmogorov length scale

$$\eta = \left(\frac{\nu^3}{\varepsilon}\right)^{1/4} \sim \left(\frac{\mu^2}{\rho^2\omega^2}\right)^{1/4} \sim \frac{T^{3/8}}{\rho^{1/2}\,\omega^{1/2}}\,,$$

where the relations $\varepsilon \approx \nu\omega^2$, $\nu = \mu/\rho$, and $\mu \sim T^{3/4}$ have been used. The streamwise and transverse vorticity components change differently at the shock. Taking the (larger) transverse components, and assuming that these change as the density jump (the RDT result), gives $\omega_{2,\mathrm{d}}/\omega_\mathrm{u} \sim \rho_\mathrm{d}/\rho_\mathrm{u}$. This yields the change at the shock as

$$\frac{\eta_\mathrm{d}}{\eta_\mathrm{u}} \approx \left(\frac{T_\mathrm{d}}{T_\mathrm{u}}\right)^{3/8} \left(\frac{\rho_\mathrm{d}}{\rho_\mathrm{u}}\right)^{-1}\,, \tag{2.1}$$

where the jumps in temperature and density can be inserted from the Rankine-Hugoniot relations. This is shown in Fig. 1, where it is clear that the Kolmogorov scale decreases

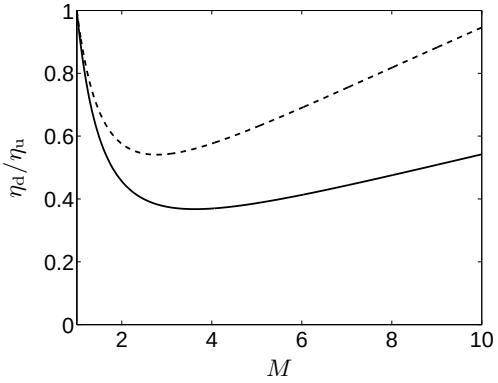

FIGURE 1. Estimated change in the Kolmogorov scale across a shock as a function of the Mach number. Eq. (2.1) with $\gamma = 1.4$ (solid) and $\gamma = 5/3$ (dashed).

across the shock. As will be seen below, the present DNS data confirms this prediction for $M \lesssim 1.9$ to reasonable accuracy. The estimate predicts that the effect becomes weaker for stronger shocks ($M \gtrsim 3.6$ for $\gamma = 1.4$), which is due to the saturation of the density jump ρ_d/ρ_u (the temperature dependence $(T_d/T_u)^{3/8}$ is essentially linear); this produces an increase at higher M. Unfortunately, the present data is not at sufficiently high Mach number to verify this prediction.

This estimated change in the Kolmogorov scale is not unexpected given the compressive nature of a shock, but, more importantly (at this stage), it has an effect on the necessary grid resolution. The present study uses grids that are refined in the streamwise direction, implying that the critical resolution is in the transverse directions. The mean Mach numbers in the present study are $M = 1.27$, 1.50 and 1.87, at which the estimated change in the Kolmogorov scale is $\eta_d/\eta_u \approx 0.72$, 0.60 and 0.48, respectively. Therefore resolution of the post-shock viscous dissipation requires twice as many grid points as resolving the pre-shock dissipation – in *every* direction.

Now, this estimate is both approximate and only valid for $k_0 x_1 \gtrsim 10$. In the region immediately behind the shock the turbulence is out of equilibrium, and the length scale of viscous dissipation is not well defined. A simple argument (the RDT result) is that the turbulence is compressed only in the streamwise direction behind the shock, which suggests that streamwise grid refinement is sufficient there. Such refinement also reduces the shock-capturing errors.

The true test of whether the grid is sufficiently fine is a systematic grid refinement. Fig. 2 shows a sample result from such a grid refinement study, in this case the vorticity variances for a case with $(M, M_t) = (1.87, 0.224)$ on successively refined grids. We note that vorticity is a sensitive quantity (given its dependence on small scales), and that other quantities converge more quickly. The figure shows that there is convergence. A close inspection reveals that the maximum difference between the two finest grids is 2%, which serves as an error estimate for the vorticity variances; quantities that depend more on the large-scale motions have lower errors. Also note that the vorticity components fail to return to isotropy on the coarsest grids.

In conclusion, the results are statistically converged to within 2% on the finest grid with $1040 \times 384^2 \approx 153 \cdot 10^6$ grid points. The fact that such a fine grid is needed even for a relatively low $Re_\lambda \approx 40$ is due to the change in the Kolmogorov scale at the shock. It will be shown below that the Taylor length scales behave differently in the present

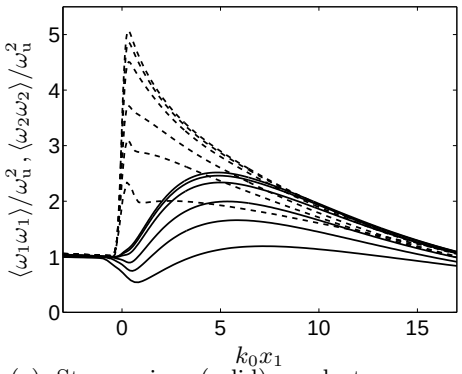

(a) Streamwise (solid) and transverse (dashed) variance.

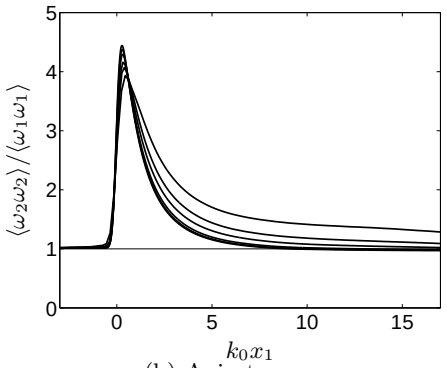

(b) Anisotropy.

FIGURE 2. Convergence of vorticity under grid refinement for $(M, M_t) = (1.87, 0.224)$. Grids with 174×64^2, 261×96^2, 347×128^2, 521×192^2, 694×256^2 and 1040×384^2 points, where finer grids yield higher variances and faster return to isotropy.

data compared to that of Lee *et al.* (1997); this difference is most likely due the better resolution of the post-shock turbulence.

3. Average results

Once the initial transients have disappeared, averages are collected over the transverse directions and a period of time $k_0\, u_{1,\rm u}\, t_{\rm stats} \approx 100$. The computed averages change little when decreasing the averaging period by half, thus confirming that the averages are converged.

There are many possible ways to non-dimensionalize the streamwise coordinate, both by turbulence length scales and convected turbulence time scales (e.g., collapsing the decay). Here we choose to scale the streamwise coordinate by the wavenumber of peak energy k_0 in order to facilitate comparison with linear analysis. In all figures the streamwise coordinate has been shifted such that the average position of the shock is at $x_1 = 0$. With this shift, the inflow is at $k_0x_1 \approx -8$, the outflow is at $k_0x_1 \approx 42$ and the sponge region begins at $k_0x_1 \approx 30$. The transverse domain size is $k_0L_{2,3} = 8\pi$.

3.1. *Mean profiles*

The mean profiles of density and velocity are shown in Fig. 3. While not shown, the pressure profiles are qualitatively similar to the density ones. The jumps at the shock are consistently smaller than the laminar Rankine-Hugoniot relations, and the deviations from the laminar jumps increase for larger values of M_t. The profiles of density and pressure show the same qualitative structure: first the jump at the shock, then a small decrease, and finally a slow increase downstream (the velocity profiles show the opposite behavior). The slow increase behind the shock is sensitive to the exact implementation of the downstream boundary condition. In the present study, non-reflecting boundary conditions based on a linearization around the laminar post-shock state are used, which may explain why all profiles approach the laminar state downstream. Therefore the downstream development of the mean quantities should not be taken as the truth. Disregarding the downstream development, all profiles still show an overshoot

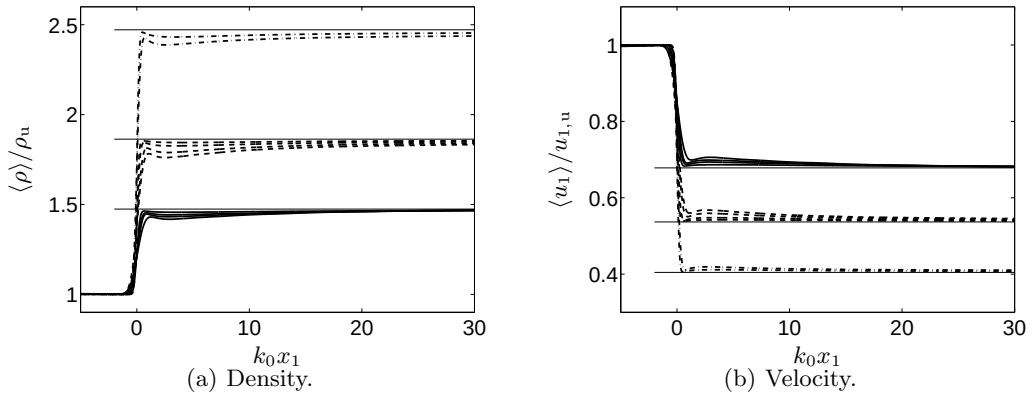

(a) Density. (b) Velocity.

FIGURE 3. Mean profiles for all cases, with thin horizontal lines denoting the laminar post-shock states. Mean Mach numbers $M = 1.27$, 1.50, 1.87 (larger M corresponds to larger shock jumps). Turbulent Mach numbers $0.16 \leq M_t \leq 0.39$, where cases with low M_t are closer to the laminar states. The pressure profiles (not shown) are qualitatively similar to the density profiles.

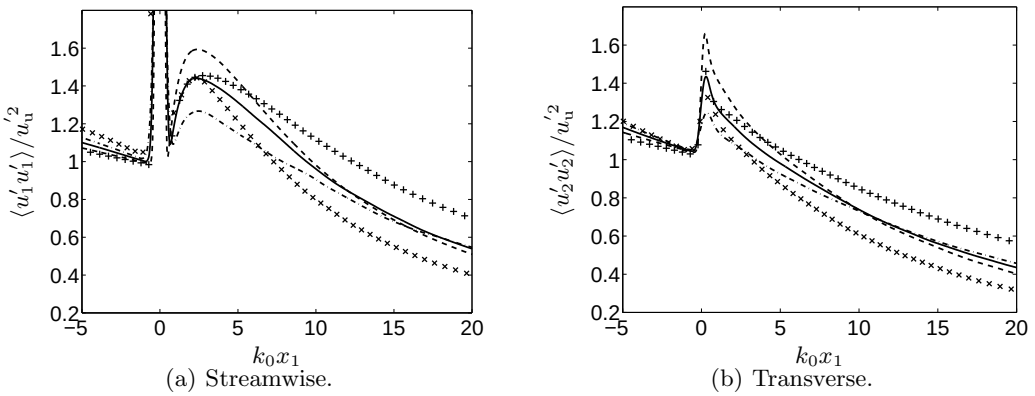

(a) Streamwise. (b) Transverse.

FIGURE 4. Velocity variances. Base case $(M, M_t) = (1.50, 0.221)$ (solid). Effect of changing M shown in lines: $M = 1.27$ (dash-dotted) and $M = 1.87$ (dashed). Effect of changing M_t shown in symbols: $M_t = 0.155$ (plus) and $M_t = 0.313$ (cross).

immediately behind the shock. Thus, on average, there is a compression at the shock followed by a slight expansion.

The deviation from the laminar shock jumps was analyzed by Lele (1992), who derived the turbulent jump conditions and used RDT to approximately close them. Lele's theory is qualitatively consistent with the present results in that increased M_t leads to smaller jumps in density and pressure (for fixed M).

3.2. *Velocity variances*

The velocity variances are shown in Fig. 4 for a set of cases where either the mean or turbulent Mach numbers are held constant. The effect of increasing the mean Mach number is to increase the amplification of both the streamwise and transverse Reynolds stresses. This is consistent with linear analysis at these Mach numbers (cf. Lee *et al.* 1997). The large peak of $\langle u_1'u_1'\rangle$ around the mean shock location is an effect of the

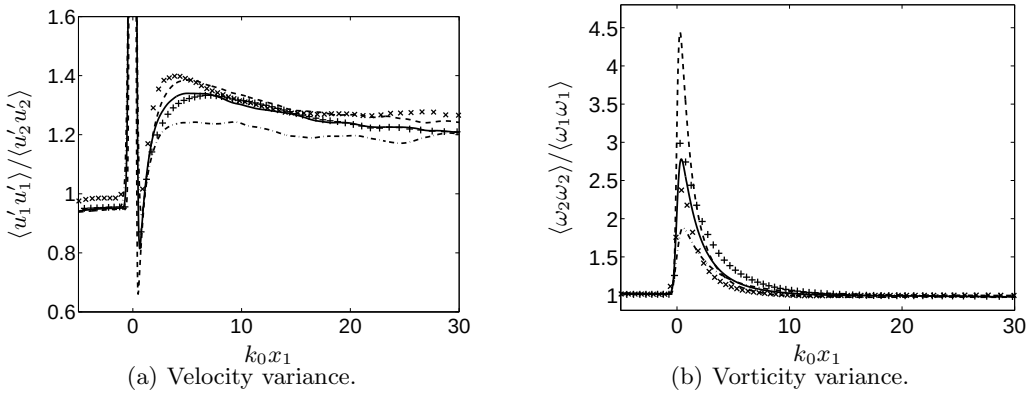

(a) Velocity variance. (b) Vorticity variance.

FIGURE 5. Anisotropy in velocity and vorticity variances. Lines/symbols as in Fig. 4.

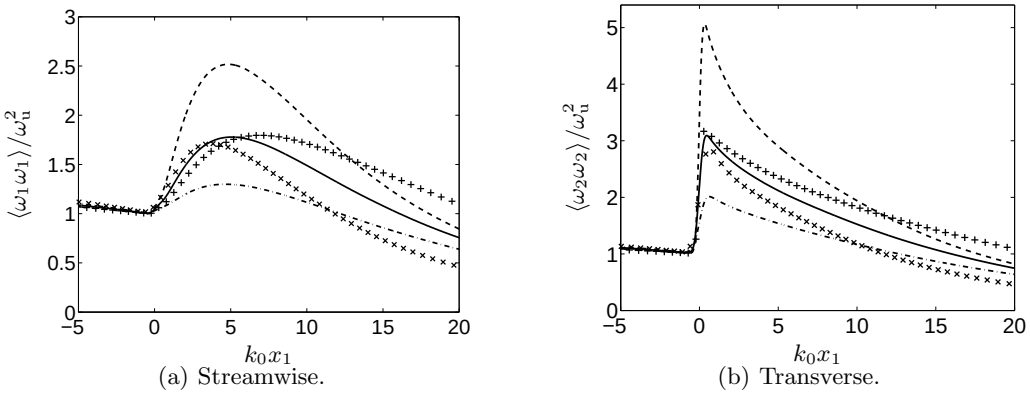

(a) Streamwise. (b) Transverse.

FIGURE 6. Vorticity variances. Lines/symbols as in Fig. 4.

unsteady shock; the width of this peak closely corresponds to the width of the shock as defined from the mean dilatation profile.

The effect of increasing the turbulent Mach number appears to be a decrease in the amplification of both components, although the rather rapid viscous decay makes any conclusive statement difficult.

The anisotropy of the Reynolds stresses $\langle u_1'u_1'\rangle/\langle u_2'u_2'\rangle$ is shown in Fig. 5, where it is clear that the shock-interaction causes the turbulence to become anisotropic (in fact, axisymmetric). There is no evidence of a return-to-isotropy in the numerical results, implying that this process, if present, is significantly slower than the viscous decay. Comparison to the results by Lee *et al.* (1997) shows a somewhat faster adjustment behind the shock, which is either due to the fully developed upstream turbulence in the present study having more fine-scale features (with shorter length/time scales) or an effect of insufficient post-shock resolution in their results.

3.3. *Vorticity variances*

The vorticity variances are shown in Fig. 6 for the same cases. The transverse vorticity is amplified directly at the shock, and then decays. The streamwise vorticity is initially unaffected by the shock, but then quickly increases until it equilibrates with the transverse

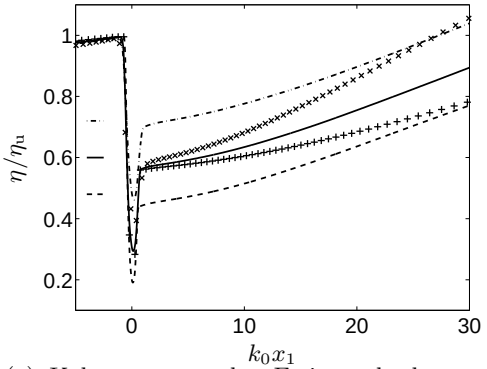

(a) Kolmogorov scale. Estimated changes from Eq. (2.1) shown in short lines at left. Lines/symbols as in Fig. 4.

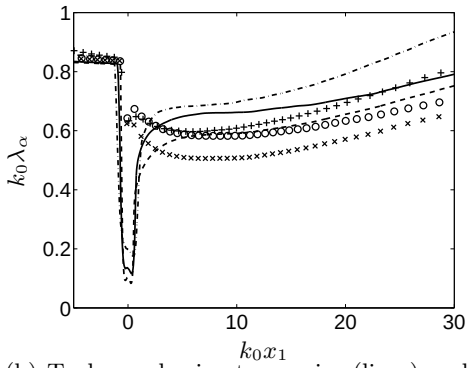

(b) Taylor scales in streamwise (lines) and transverse (symbols) directions. Base case $(M, M_t) = (1.50, 0.221)$ (solid, circle). Changing to $M = 1.87$ (dashed, cross); changing to $M_t = 0.313$ (dash-dotted, plus).

FIGURE 7. Kolmogorov and Taylor length scales.

components. Fig. 5 shows that there is a clear return to (local) isotropy for the vorticity components at $k_0x_1 \approx 10$. This is in contrast to earlier work by Lee *et al.* (1997), where the transverse vorticity was still 50% larger than the streamwise at $k_0x_1 \approx 12$ (the end of their domain). The most likely explanation for this difference is the grid resolution. It was shown in Fig. 2(b) that the vorticity components fail to return to isotropy when the post-shock turbulence is under-resolved. Since the post-shock vorticity evolution is a nonlinear process, where transverse vorticity is tilted into the streamwise direction, one can hypothesize that insufficient grid resolution inhibits this process.

The effect of increasing the mean Mach number is simply to increase the amplification of both components. The effect of increasing the turbulent Mach number is, again, difficult to discuss in any detail, given the rapid viscous decay.

3.4. *Length scales*

Given the efforts to ensure similar turbulent states upstream of the shock for all cases, the pre-shock Kolmogorov and Taylor scales are essentially similar for all cases. The values are $k_0\eta_u \approx 0.0682$ (within 2% for all cases) and $k_0\lambda_u \approx 0.842$ (within 1% for all cases), respectively. The profiles of these length scales are shown in Fig. 7 for some representative cases.

The Kolmogorov scale decreases at the shock and immediately begins growing. In section 2.3 it was estimated that the change at the shock should be $\eta_d/\eta_u \approx 0.72, 0.60$ and 0.48 at the three mean Mach numbers, respectively; these levels are marked in Fig. 7(a). Since the turbulence is locally anisotropic and out of equilibrium for $0 \lesssim k_0x_1 \lesssim 10$, and since the Kolmogorov scale grows in the streamwise direction, it is not clear exactly at what location one should test the predicted η_d/η_u. A simple extrapolation to the mean shock position yields $\eta_d/\eta_u \approx 0.68, 0.54$ and 0.43 at the three Mach numbers, respectively. Hence the estimate captures the key trend, albeit with a slight (but consistent) over-prediction.

The Taylor scales show a perhaps surprising behavior: while both streamwise and transverse scales decrease at the shock, the streamwise scale quickly becomes larger than the transverse one for all cases considered here. At first sight this is counterintuitive,

since the shock is essentially a 1-D compression. It also disagrees with linear analysis (cf. Lee *et al.* 1997), which predicts $\lambda_1 < \lambda_2$. The DNS results of Lee *et al.* (1993, 1997) were varied; the streamwise scale was larger for some cases while smaller for others.

This issue is best resolved by considering the definition of the Taylor scale

$$\lambda_\alpha = \sqrt{\frac{\langle u'_\alpha u'_\alpha \rangle}{\langle (\partial_\alpha u'_\alpha)^2 \rangle}} \quad \text{(no summation)}\,. \tag{3.1}$$

In Fig. 5 it was shown that the vorticity components become isotropic at $k_0 x_1 \approx 10$. This suggests that the full velocity gradient tensor is also isotropic at this point; direct evaluation confirms this. Thus the denominators in the streamwise and transverse Taylor scales are similar. Fig. 5 also shows that the Reynolds stresses do not reach isotropy; it follows immediately that $\lambda_1 > \lambda_2$. Therefore the present results in Fig. 7(b) make sense, as do the earliest results by Lee *et al.* (1993). The question is why linear theory and the later results by Lee *et al.* (1997) disagree with this?

The return to local isotropy is a nonlinear process of vortex tilting; this process is absent from linear theory, and the length scales coming out of the theory do not include this process. This explains why linear theory disagrees with the present results.

While the calculations by Lee *et al.* (1997) resolved the viscous scales of the incoming turbulence, computer limitations prevented the resolution of the post-shock turbulence. As discussed above, this implied that $\langle \omega_2 \omega_2 \rangle$ was 50% higher than $\langle \omega_1 \omega_1 \rangle$ at the end of their domain. Assuming that this lack of isotropy in the vorticity components was accompanied by a similar lack of isotropy of the velocity gradients, i.e., $\partial_1 u_1 > \partial_2 u_2$, this would yield a too small λ_1. It is tempting to argue that the failure to fully resolve the post-shock region (in that study) essentially under-predicted the nonlinear processes behind the shock, thus producing results closer to those from linear theory. This is speculative, but would explain the excellent agreement between linear theory and the results of Lee *et al.* (1997).

The earlier study by Lee *et al.* (1993) contains some support for this hypothesis: their most highly resolved case (at $M = 1.2$) showed $\lambda_1 > \lambda_2$ toward the end of the domain, i.e., a similar result as in the present study.

We should finally note that linear theory predicts that $\langle u'_1 u'_1 \rangle$ is larger than $\langle u'_2 u'_2 \rangle$ for low values of M, but that the opposite holds for high M. If true far behind the shock (after the return to local isotropy), this would imply that the streamwise microscale would become smaller than the transverse at high enough Mach number. The present data is not at sufficiently high M to resolve this issue.

4. Instantaneous results

We next investigate the instantaneous structures of the shock/turbulence interaction, and how these are affected by the turbulent Mach number. On average the turbulence causes the shock jumps in density, pressure and velocity to be smaller than the laminar Rankine-Hugoniot conditions, but the instantaneous picture is more complex. In this section we visualize and investigate some instantaneous structures. Specifically, we compare instantaneous interactions that are "strong" and "weak" in the sense that they have fluid compressions and density/pressure jumps that are larger or smaller than on average. Starting with an instantaneous field, the dilatation at the shock is defined as

$$\theta_{\text{shock}}(x_2, x_3) = \min_{x_1} \theta(x_1, x_2, x_3)\,.$$

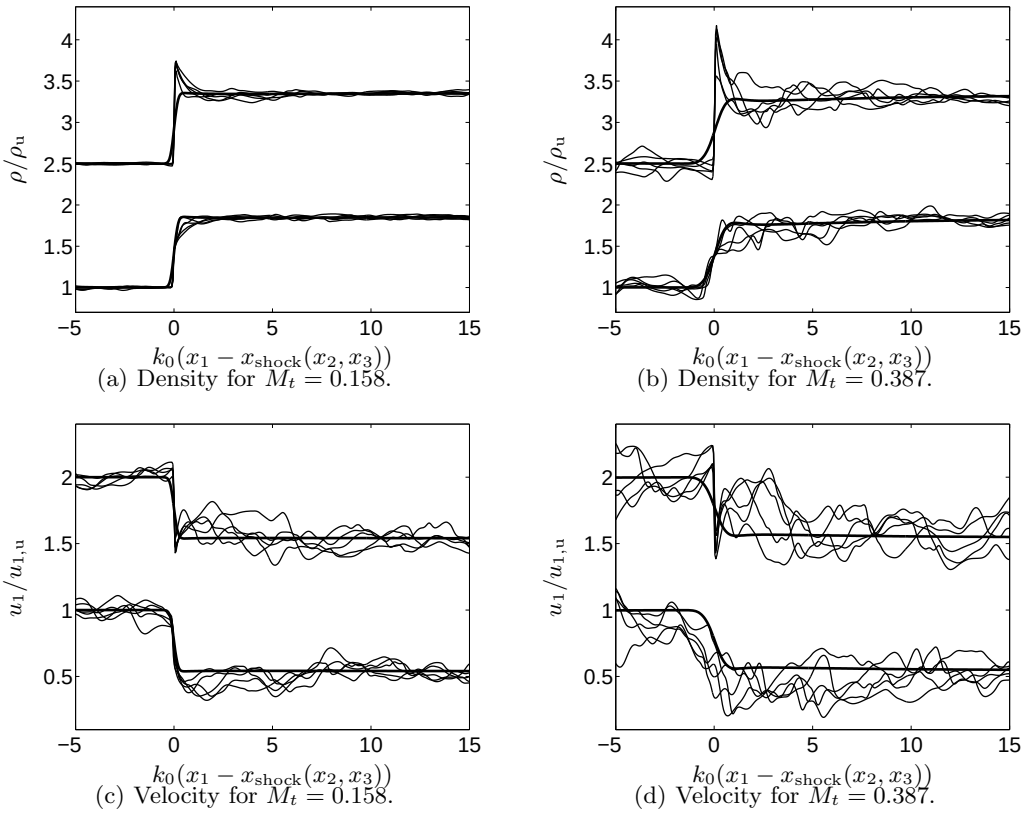

(a) Density for $M_t = 0.158$. (b) Density for $M_t = 0.387$.

(c) Velocity for $M_t = 0.158$. (d) Velocity for $M_t = 0.387$.

FIGURE 8. Instantaneous profiles along the streamwise direction for $M = 1.50$ at different transverse coordinates (x_2, x_3). Each figure shows five profiles through "weak" and "strong" (with offset) interactions, respectively. The streamwise coordinate has been shifted by the instantaneous position of the shock $x_{1,\mathrm{shock}}(x_2, x_3)$ for each profile. Mean profiles shown by thick lines.

We then find the points (x_2, x_3) of the strongest/weakest interaction as the min/max of θ_{shock}. After excluding a circle near these points, the process is repeated to find the next strongest/weakest points, and so on. Profiles through the five strongest/weakest interaction points are shown in Fig. 8 at two different turbulent Mach numbers: $M_t = 0.158$ and 0.387, corresponding to turbulence intensities of 6% and 15%, respectively. For clarity, the streamwise coordinate x_1 has been shifted in the figures such that the instantaneous shock-positions line up. We note that the resulting "strong" and "weak" profiles closely resemble the "peaked" and "rounded" ones found by Hesselink & Sturtevant (1988).

We first note that the high-intensity case (naturally) displays much larger excursions from the mean, and that the mean shock thickness is larger. The stronger-than-average interactions are qualitatively similar at both values of M_t. The instantaneous density jump is larger than the average, in fact almost twice as large for the $M_t = 0.387$ case, and there is an immediate expansion and decrease of ρ behind the shock toward the mean level. This expansion is also seen in the velocity profiles, which all show positive streamwise acceleration both upstream and (especially) downstream of the shock. Apart from explaining the post-shock decrease in density, this acceleration also suggests that the stronger-than-average interaction is associated with eddy structures that locally ac-

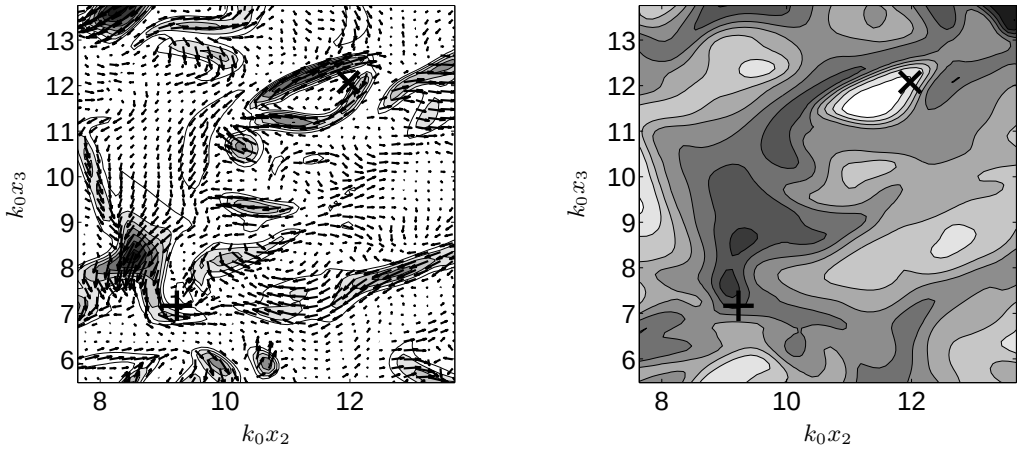

(a) Contours and vectors of vorticity. (b) Contours of streamwise velocity.

FIGURE 9. Instantaneous slice immediately behind the shock (looking upstream) for $(M, M_t) = (1.50, 0.387)$, with dark regions denoting higher values. The locations of one instantaneously strong (plus at $\approx (9, 7)$) and one weak (cross at $\approx (12, 12)$) interaction are also marked.

celerate the fluid. The fact that the acceleration appears stronger behind the shock would be consistent with an eddy oriented in the transverse plane, since the shock compression would increase the transverse vorticity (and thereby the induced acceleration).

To investigate this hypothesis we consider the transverse vorticity in a slice immediately behind the shock in Fig. 9. The slice is taken from the same snapshot as the profiles in Figs. 8(b) and 8(d); the locations of one strong and one weak interaction are also shown in Fig. 9.

Both the strong and weak interactions occur near strong eddies. The weak interaction, in particular, occurs near the head of a hairpin- or ring-like eddy. The vorticity vectors in Fig. 9(a) show that the eddy near the weak point acts to decrease the streamwise velocity, while the eddy near the strong interaction acts to increase it. This leads to low- and high-speed jets, as shown in Fig. 9(b). Therefore the hypothesized relationship between strong transverse eddy structures, local acceleration and instantaneously strong/weak shock-interactions seems reasonable.

A further visualization is shown in Fig. 10 for the same case. The shock displays two structures that do not occur at lower M_t in the region around $(k_0x_1, k_0x_2) \approx (0, 13)$. First, there is a region of low momentum where the shock is instantaneously replaced by a smooth compression (a "weak" interaction). Secondly, the shock has branched out in a Y-shape immediately above this low-momentum region.

5. Summary and future work

A sequence of direct numerical simulations (DNS) of canonical shock/turbulence interaction is presented. Care is taken to ensure fully developed isotropic turbulence upstream of the shock, and a systematic grid refinement study shows that the viscous dissipation is fully resolved on the finest grids. Thus the DNS databases are ideally suited for exploration of the fundamental physics and dynamics of shock/turbulence interaction.

It is argued that previous DNS studies of this problem may have been under-resolved

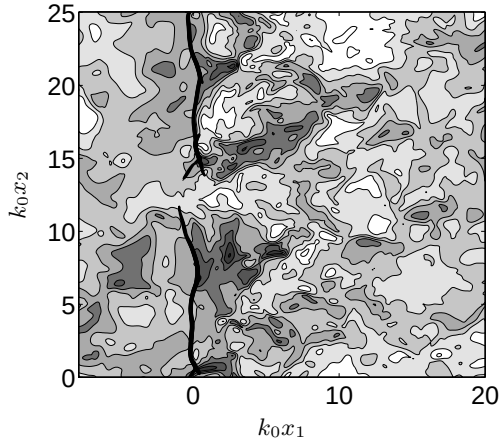

FIGURE 10. Instantaneous slice for $(M, M_t) = (1.50, 0.387)$. Streamwise momentum ρu_1 in gray scale, with dark regions denoting higher momentum. Contours of high fluid compression (outlining the shock) are overlaid in thick lines.

in the post-shock region, since the Kolmogorov scale decreases during the interaction. A simple estimate of this change is given; it agrees to reasonable accuracy with the DNS data. A more quantitative assessment would require higher Reynolds numbers, since the viscous decay is significant in the present data. The estimate suggests a smaller change in the Kolmogorov scale at Mach numbers above 3.6, which should be investigated in future work.

Contrary to the previous DNS by Lee *et al.* (1997), and contrary to the linear interaction analysis of Ribner (1954), the streamwise Taylor length scale is consistently larger than the transverse scale in the present data. While the present result is somewhat counterintuitive, it is entirely consistent with the notion of a return to local isotropy at the smallest scales, and the lack of a return to isotropy at the larger scales. These processes are nonlinear, and therefore absent from linear analysis. It is speculated that under-resolution in the post-shock region may have under-predicted this nonlinear development in previous DNS studies.

Instantaneous profiles through the shock can be quite different from the average profiles, especially at higher levels of the turbulent (compared to the mean) Mach number. Locally, the shock compression may be twice as strong as on average, or so weak that it is effectively a smooth compression. It is conjectured that these excursions from the average behavior can be connected to local eddy structures with strong transverse vorticity that cause local acceleration/deceleration that the shock responds to.

The most important future work is to analyze the data in more depth, and more quantitatively. The amplification ratios of velocity and vorticity variances should be compared to linear analysis, and the instantaneous flow-fields around extreme interaction events should be probed in greater detail.

Acknowledgments

Financial support has been provided by the Department of Energy Scientific Discovery through Advanced Computing (SciDAC) program and the Natural Sciences and Engineering Research Council of Canada. The fine-grid calculations were run at the National Energy Research Scientific Computing Center under the ERCAP program.

REFERENCES

Ducros, F., Laporte, F., Souleres, T., Guinot, V., Moinat, P. & Caruelle, B. 2000 High-order fluxes for conservative skew-symmetric-like schemes in structured meshes: application to compressible flows. *J. Comput. Phys.* **161**, 114–139.

Hesselink, L. & Sturtevant, B. 1988 Propagation of weak shocks through a random medium. *J. Fluid Mech.* **196**, 513–553.

Larsson, J. 2008 Blending technique for compressible inflow turbulence: algorithm localization and accuracy assessment. *J. Comput. Phys.* (in press).

Larsson, J. & Gustafsson, B. 2008 Stability criteria for hybrid difference methods. *J. Comput. Phys.* **227**, 2886–2898.

Larsson, J., Lele, S. K. & Moin, P. 2007 Effect of numerical dissipation on the predicted spectra for compressible turbulence. *Annual Research Briefs*, Center for Turbulence Research, Stanford, CA, 47–57.

Lee, S., Lele, S. K. & Moin, P. 1993 Direct numerical simulation of isotropic turbulence interacting with a weak shock wave. *J. Fluid Mech.* **251**, 533–562.

Lee, S., Lele, S. K. & Moin, P. 1997 Interaction of isotropic turbulence with shock waves: effect of shock strength. *J. Fluid Mech.* **340**, 225–247.

Lele, S. K. 1992 Shock-jump relations in a turbulent flow. *Phys. Fluids* **4** (12), 2900–2905.

Pirozzoli, S. 2002 Conservative hybrid compact-WENO schemes for shock-turbulence interaction. *J. Comput. Phys.* **178**, 81–117.

Pope, S. B. 2000 *Turbulent Flows*, Cambridge University Press, Cambridge, UK.

Ribner, H. S. 1954 Shock-turbulence interaction and the generation of noise. NACA Report 1233.

Ristorcelli, J. R. & Blaisdell, G. A. 1997 Consistent initial conditions for the DNS of compressible turbulence. *Phys. Fluids* **9** (1), 4–6.

Xiong, Z., Nagarajan, S. & Lele, S. K. 2004 Simple method for generating inflow turbulence. *AIAA J.* **42** (10), 2164–2166.

Zank, G. P., Zhou, Y., Matthaeus, W. H. & Rice, W. K. M. 2002 The interaction of turbulence with shock waves: A basic model. *Phys. Fluids* **14** (11), 3766–3774.